

Boundaries of the Peruvian Oxygen Minimum Zone shaped by coherent mesoscale dynamics

João H Bettencourt^{1,2}, Cristóbal López¹, Emilio Hernández-García¹, Ivonne Montes^{3,6},
Joël Sudre⁴, Boris Dewitte⁴, Aurélien Paulmier^{4,5}, Véronique Garçon⁴

¹*IFISC, Instituto de Física Interdisciplinar y Sistemas Complejos (CSIC-UIB), Campus Universitat de les Illes Balears, E-07122 Palma de Mallorca, Spain.*

²*School of Mathematical Sciences, University College Dublin, Dublin 4, Ireland.*

³*GEOMAR, Helmholtz-Zentrum für Ozeanforschung Kiel, Wischhofstr. 1-3, 24148 Kiel, Germany.*

⁴*LEGOS, Laboratoire d'Etudes en Géophysique et Océanographie Spatiales, 18, av. Edouard Belin, 31401 Toulouse Cedex 9, France.*

⁵*IMARPE, Instituto del Mar de Perú, Esquina Gamarra y General Valle S/N, Chucuito, Callao, Perú.*

⁶*IGP, Instituto Geofísico del Perú, Lima, Perú.*

Dissolved oxygen in sea water is a major factor affecting marine habitats and biogeochemical cycles¹⁻³. Oceanic zones with oxygen deficits represent significant portions of the area and volume of the oceans⁴ and are thought to be expanding^{5,6}. The

Peruvian oxygen minimum zone is one of the most pronounced and lies in a region of strong mesoscale activity in the form of vortices and frontal regions, whose effect in the dynamics of the oxygen minimum zone is largely unknown. Here, we study this issue from a modeling approach and a Lagrangian point of view, using a coupled physical–biogeochemical simulation of the Peruvian oxygen minimum zone and finite-size Lyapunov exponent fields to understand the link between mesoscale dynamics and oxygen variations. Our results show that, at depths between 380 and 600 meters, mesoscale structures have a relevant dual role. First, their mean positions and paths delimit and maintain the oxygen minimum zone boundaries. Second, their high frequency fluctuations entrain oxygen across these boundaries as eddy fluxes that point towards the interior of the oxygen minimum zone and are one order of magnitude larger than mean fluxes. We conclude that these eddy fluxes contribute to the ventilation of the oxygen minimum zone.

Regions of the ocean with strong O_2 deficiency in the water column are called Oxygen Minimum Zones (OMZs). The OMZs are differentiated in the vertical by three distinct layers: the oxycline (upper O_2 gradient), the core (typically with $O_2 < 20 \mu M$) and the lower O_2 gradient. The Eastern Tropical South Pacific (ETSP) contains one of the three major permanent OMZ, with an oxycline extending from the upper 10 to 170 meters, a core with a thickness of around 400 meters⁴ and lower oxygen gradient extending to about 3700 meters⁴. This OMZ is maintained by the combination of signif-

icant rates of biological production and decomposition of sinking organic material⁷ at the Peruvian upwelling region, and weak circulation in the shadow zone of the southern Pacific subtropical gyre. The circulation is then dominated by the equatorial and eastern boundary current systems^{8,9}. Energetic vortices, called mesoscale eddies, and filaments are ubiquitous in this area¹⁰. In contrast to the oligotrophic regions of the ocean where mesoscale eddies can sustain biological productivity¹¹, in upwelling regions stirring by eddies – the process of tracer gradient intensification by advection – tends to inhibit biological production^{12,13}.

In the ETSP, the role played by mesoscale structures in the distribution of O₂ within the OMZ remains unclear and we approach this issue by analyzing data from a coupled physical-biogeochemical high-resolution model¹⁴ of the regional ETSP (see Methods), and characterizing mesoscale transport and stirring by means of Finite-size Lyapunov exponent (FSLE) fields^{15,16} (see Methods and Supplementary Information). Maxima in these fields form thin filamentary structures, the so-called Lagrangian Coherent Structures (LCS)^{16–18} identifying the most intense mesoscale regions and acting as barriers for fluid transport across them.

In this work we focus on the transport aspects of the mesoscale-OMZ interaction, particularly in the OMZ boundaries, and the fluxes across them. We do not address specifically the biogeochemical processes occurring inside the zone which are certainly determinant (and are included in our regional simulation model) but we gauge instead

the physical effects of the mesoscale structures on the OMZ dynamics. This is done by: a) computing correlations between the (temporally averaged) O₂ concentration and FSLE at layers located at different depths; b) studying events of O₂ rich-waters entrainment into the OMZ; c) calculating the temporal average of O₂ normal fluxes across the northern and southern boundaries of the OMZ as a function of depth, and its correlation with the average mixing measurement obtained from FSLE. The outcome of these analyses is that, despite the important biogeochemical processes, mesoscale stirring already determines many important features of the oxygen distribution.

The 20 μM isosurface of the annual mean O₂ field for simulation year (s.y.) 21 (Fig. 1a) gives an OMZ core with maximal horizontal extension at approximately 400 m depth extending between 3° S and 16° S. The higher O₂ concentrations north of 2° S are associated with eastward equatorial subsurface currents carrying relatively oxygen-rich water^{19,20}, while the southern increase of O₂ (14° S to 17° S) is adjacent to the northern part of the subtropical gyre. Figure 1a also displays the annual mean backward FSLE field at 410 m depth, which shows a high correlation with the mean O₂ field delineating the limits of the OMZ core. The FSLE mean field is structured as zonal bands coincident with the north and south OMZ boundaries with relatively high FSLE values when compared to the core region. Both bands signal stirring by the eddies formed at the continental shelf and advected offshore, and by other mesoscale processes^{10,20}. This indicates that the enhanced mesoscale activity in those areas delineates the limits of the

average OMZ core region.

Since LCS (that we locate as maximum values of FSLE) act as transport barriers, large gradients of O₂ should occur across them²¹. Thus we expect to find a relationship between the stirring intensity as measured by the FSLE and the O₂ gradient norm (see additional discussion in Supplementary Information; in the following, the term O₂ gradient refers to the norm). The relationship between both fields is quantified in Fig. 1b where we plot the latitudinal variation between 18° S and 2° N of mean FSLE and O₂ gradient averaged between the coast and 85°W and from 380 to 600 m depth, showing the coincidence in the maxima of both quantities: the maxima of FSLE indicating the positions of the LCS and the maxima of the O₂ gradient signalling the northern and southern boundaries of the OMZ. This correlation is not equally strong at all depths as it is shown in Fig. 1c, where we plot the vertical profile of the Pearson correlation coefficient²², R , between the zonally averaged mean FSLE and mean O₂ gradient. Roughly, we can distinguish two areas in the OMZ core: a) between 190 – 350 meters where these quantities show correlations of alternating sign; and b) between 380 – 600 meters where the correlation is large and positive (with an average R of 0.748). It is in this subregion of the OMZ core that its boundaries are strongly determined by the mesoscale dynamics. This is so because the OMZ dynamics is a balance between hydrodynamic and biogeochemical processes. At these depths, the physical forcing, albeit lower than in the upper layers, has a variability two orders of magnitude larger than the

biogeochemical forcing ¹⁴ (see Supplementary Information) and its effects are clearly visible in the strong correlation between FSLE and O₂ gradients.

Besides mean behaviour, individual events are also relevant, since mesoscale eddies are able to transport waters with different biogeochemical properties with respect to surrounding areas, giving rise to sporadic episodes of high O₂ patches inside the OMZ. Fig. 2 shows one of these temporal sequences where an eddy dipole (with borders signalled by maxima of FSLE at 410 meters) entrains water with high oxygen content (the red-yellow tongue at 80 – 82°W) towards the interior of the OMZ. This episode had a duration of approximately 3 months (9/9 to 1/12 of s.y. 21; first month displayed) and during this period the entrainment of these waters carried 0.4×10^6 mol of O₂ per meter of depth into the OMZ at this depth. Episodes of this nature are frequent at the southern boundary although often less intense (see Supplementary Information). At the northern boundary the frequency of O₂ injection episodes is higher and they last longer. The difference between both boundaries rests upon the spatial distribution of O₂. Since the mean northern boundary is almost coincident with the large O₂ gradient region most of the time, any small displacement of this region will cause a significant change in the O₂ signal right at the boundary. In the southern border gradients are more distributed and strong anomalous O₂ signals will be caused only by the mesoscale eddies entraining water across the boundary as in Fig. 2. At both boundaries the episodic ventilation of the OMZ follows an offshore path consistent with the propagation of eddies and other

perturbations from the coastal waters to the open ocean. A characterization of FSLE and O_2 joint dynamics in terms of wavelet spectra, emphasizing the dominant periods, is presented in the Supplementary Information.

The average amount of O_2 entering through the OMZ boundaries due to mesoscale processes was quantified by computing eddy fluxes of O_2 normal to the northern and southern limits. Small-scale turbulent diffusion produces much smaller fluxes. Eddy fluxes were calculated across the mean $20 \mu M$ level boundary between 200 and 600 meters of depth during s.y. 21, from the covariance between velocity anomalies and O_2 concentration anomalies (see Supplementary Information). Vertical fluxes across these borders were always orders of magnitude smaller than horizontal ones (see Supplementary Information), and thus the following discussion about horizontal components does also apply to the total normal flux. At the northern boundary the horizontal eddy flux profile is mainly positive (Fig. 3a, red line), meaning that the O_2 variance due to horizontal eddy fluxes is bringing O_2 into the OMZ. The highest eddy fluxes are reached at core depths between 350 and 500 meters which is close to the depth range where the higher FSLE mean values at the boundary are obtained (Fig. 3a, blue line), although the maximum value of this latter quantity (associated to the presence of the subsurface currents^{19,20}) appears deeper than the eddy flux maximum (350 vs 480 meters). Above 300 meters the horizontal eddy fluxes are small and the minimum is obtained around 300 meters, where the FSLE is also minimum. Globally integrated between 200-600

m depth and along the northern $20 \mu M$ boundary from coast until $88^\circ W$, the horizontal eddy flow rate towards the OMZ interior is of $6.15 \times 10^6 \mu mol s^{-1}$, whereas the corresponding mean flow rate is $2 \times 10^5 \mu mol s^{-1}$ and directed outwards (see Supplementary information). At the southern $20 \mu M$ mean boundary, eddy fluxes are also positive (Fig. 3b) along the range of depths considered, being fairly constant from 200 to 300 m, and nearly vanishing between 400 to 600 m depth. Integrating between 200-600 m from coast to $88^\circ W$, the eddy flow rate towards the OMZ interior is of $1 \times 10^7 \mu mol s^{-1}$, whereas the mean flow rate is $3.56 \times 10^5 \mu mol s^{-1}$ and directed outwards (see Supplementary Information).

The differences in the O_2 eddy fluxes between the northern and southern boundaries may be understood in terms of the mesoscale activity. In the southern boundary O_2 anomalies are caused by eddies (signalled by large FSLE) crossing the boundary. Thus higher O_2 eddy fluxes should be associated with higher FSLE values, which indeed is true looking at the profiles in Fig.3b). On the northern boundary, this holds until the local minimum at 312 m. Below this depth, O_2 anomalies crossing the northern border are mainly related to, as stated above, fluctuations in the position of a large O_2 gradient zone, associated to fluctuations in the subsurface equatorial currents, separating the subsurface O_2 rich equatorial waters from the OMZ core.

To conclude, in this work we have addressed the role of mesoscale structures that populate the OMZ in the ETSP. We identified the boundaries of these mesoscale ed-

dies and fronts as LCS that act as barriers to transport controlling fluid interchange in and out the OMZ. Comparison of the FSLE approach with an exit time characterization (see Supplementary Information) supports this view. Despite the important biogeochemical processes, mesoscale stirring already shapes important features of the oxygen distribution. We find that mesoscale dynamics plays a dual role, which can be respectively associated with the average behaviour and with the turbulent fluctuations. The northern and southern boundaries of the OMZ core are well determined by the averaged mesoscale dynamics, in particular for depths between 300 and 600 meters, where a good correlation between mean FSLE and O_2 gradients was found. At other depths the relation between FSLE and O_2 may not hold, indicating significant O_2 forcing by biogeochemical processes. Episodic events of OMZ ventilation are produced by eddy stirring where waters with high O_2 content are entrained into the OMZ by the action of mesoscale eddies. On the whole, between 200 and 600 m depth, eddy fluxes were found to bring O_2 inside the OMZ at both the northern and southern frontiers, while O_2 mean fluxes were much smaller and in the opposite direction. The biogeochemical processes occurring in the interior of the OMZ would provide the dominant oxygen consumption sink to close the O_2 budget and maintain the OMZ core.

Methods

Circulation and OMZ modeling

The circulation and OMZ modeling in the Eastern Tropical Pacific was accomplished by the combination of the hydrodynamic model ROMS²³ (Regional Ocean Modeling System) and the biogeochemical model developed²⁴ for the Eastern Boundary Upwelling Systems (BioEBUS). The Eastern Tropical Pacific configuration covers the region from 4° N to 20° S and from 70° to 90° W with an horizontal resolution of 1/9° degrees (\approx 12 km) and 32 terrain-following vertical levels with variable vertical resolution (higher in the upper ocean). The coupled model is run in a climatological configuration previously validated²⁵ for the Eastern Tropical South Pacific, and the present configuration has been recently validated and a sensitivity analysis performed¹⁴. The model was forced by the QuickSCAT²⁶ wind stress monthly climatology and by heat and fresh water fluxes from the COADS²⁷ monthly climatology. The dynamical variables at the three open ocean boundaries are provided by a monthly climatology computed from the Simple Ocean Data Assimilation reanalysis²⁸. For the biogeochemical model, boundary conditions of nitrate and oxygen concentrations are taken from CSIRO Atlas of Regional Seas (CARS 2009, <http://www.cmar.csiro.au/cars>) and chlorophyll a concentration from SeaWiFS (<http://oceancolor.gsfc.nasa.gov/>). The simulations were performed for a 22-year period. The first 13 years were run with the physics only and the following 9-years were run with the physical/biological coupling. The coupled model reached a statistical

equilibrium after 4 years and model outputs were then stored every 3 days (averaged).

Finite-size Lyapunov exponent

The Finite-size Lyapunov exponent (FSLE), λ , is a measure of the rate of divergence in the positions of particle pairs while separating from an initial distance δ_0 up to a final distance δ_f . It was developed to study non-asymptotic dispersion processes¹⁵ and to quantify dispersive behavior of particles, especially in those cases where length scales are easier to identify than temporal ones. It is given by the following expression:

$$\lambda = \frac{1}{\tau} \log \frac{\delta_f}{\delta_0},$$

where τ is the time needed for the initial separation to increase from δ_0 to δ_f . The FSLE is a function of the initial and final separations, and also of the initial location of the particle pair \mathbf{x}_0 and of the time of release t_0 . Thus, the computation of λ for a given set of initial locations and in a time interval provides an insight to the locations of weaker/stronger particle dispersion and its evolution with time in the domain D . In fluid flows, regions that exhibit substantial stretching of fluid material, hence high values of λ , have filamental shapes and have been associated with barriers and avenues to transport¹⁶ that strongly constrain the mixing of fluid with different properties, the so-called LCS^{16–18}. Trajectory integration can be done from the present to the future, forward in time, or towards the past, backwards in time. The locations with high values of the backwards Lyapunov field are the structures better delimiting the distribution of transported sub-

stances and providing barriers to transport^{16,18}. Thus, the FSLE backwards field is the one used in this paper.

To compute the three-dimensional FSLE field we extended a previous two-dimensional method¹⁶ to include the third dimension, by computing the time τ it takes for particles initially separated by $\delta_0 = (\Delta x_0^2 + \Delta y_0^2 + \Delta z_0^2)^{1/2}$ to reach a final distance of $\delta_f = (\Delta x_f^2 + \Delta y_f^2 + \Delta z_f^2)^{1/2}$. However, in a similar application for the Benguela upwelling system²⁹ it was observed that the displacement in the vertical z direction does not contribute significantly to the calculation of δ_f and so we define a quasi-3d computation of FSLE: we use the full three dimensional velocity field for particle advection but particles are initialized in horizontal ocean layers and the contribution Δz_f is not considered when computing δ_f .

1. Gnanadesikan, A., Dunne, J. & John, J. Understanding why the volume of suboxic waters does not increase over centuries of global warming in an Earth System Model. *Biogeosciences* **9**, 1159–1172 (2012).
2. Lam, P., Lavik, G., Jensen, M., van de Vossenberg, J., Schmid, M. *et al.* Revising the nitrogen cycle in the Peruvian oxygen minimum zone. *P. Natl. Acad. Sci.* **106**, 4752–4757 (2009).
3. Ward, B., Devol, A., Rich, J., Chang, B., Bulow, S. *et al.* Denitrification as the

- dominant nitrogen loss process in the Arabian Sea. *Nature* **461**, 78–81 (2009).
4. Paulmier, A. & Ruiz-Pino, D. Oxygen minimum zones (OMZs) in the modern ocean. *Prog. Oceanogr.* **80**, 113–128 (2009).
 5. Bopp, L., Le Quere, C., Heimann, M., Manning, A. & Monfray, P. Climate-induced oceanic oxygen fluxes: Implications for the contemporary carbon budget. *Global Biogeochem. Cy.* **16**, 6–1–6–13 (2002).
 6. Stramma, L., Johnson, G., Sprintall, J. & Mohrholz, V. Expanding oxygen-minimum zones in the tropical oceans. *Science* **320**, 655–658 (2008).
 7. Chavez, F. & Messie, M. A comparison of Eastern Boundary Upwelling Ecosystems. *Prog. Oceanogr.* **83**, 80–96 (2009).
 8. Penven, P., Echevin, V., Pasopera, J., Colas, F. & Tam, J. Average circulation, seasonal cycle, and mesoscale dynamics of the Peru Current System: A modeling approach. *J. Geophys. Res.* **110**, C10021 (2005).
 9. Montes, I., Colas, F., Capet, X. & Schneider, W. On the pathways of the equatorial subsurface currents in the eastern equatorial Pacific and their contributions to the Peru-Chile Undercurrent. *J. Geophys. Res.* **115**, C09003 (2010).
 10. Chaigneau, A., Gizolme, A. & Grados, C. Mesoscale eddies off Peru in altimeter records: Identification algorithms and eddy spatio-temporal patterns. *Prog. Oceanogr.* **79**, 106–119 (2008).

11. Oschlies, A. & Garçon, V. Eddy-induced enhancement of primary productivity in a model of the North Atlantic Ocean. *Nature* **394**, 266–269 (1998).
12. Rossi, V., López, C., Hernández-García, E., Sudre, J., Garçon, V. *et al.* Surface mixing and biological activity in the four Eastern Boundary Upwelling Systems. *Nonlinear Proc. Geoph.* **16**, 557–568 (2009).
13. Gruber, N., Lachkar, Z., Frenzel, H., Marchesiello, P., Munnich, M. *et al.* Eddy-induced reduction of biological production in eastern boundary upwelling systems. *Nat. Geosci.* **4**, 787–792 (2011).
14. Montes, I., Dewitte, B., Gutknecht, E., Paulmier, A., Dadou, I. *et al.* High-resolution modeling of the Eastern Tropical Pacific Oxygen Minimum Zone: Sensitivity to the tropical oceanic circulation. *J. Geophys. Res.-Oceans* **119**, 5515–5532 (2014).
15. Aurell, E., Boffetta, G., Crisanti, A., Paladin, G. & Vulpiani, A. Predictability in the large: An extension of the concept of Lyapunov exponent. *J. Phys. A-Math. Gen.* **30**, 1–26 (1997).
16. d’Ovidio, F., Fernández, V., Hernández-García, E. & López, C. Mixing structures in the Mediterranean Sea from finite-size Lyapunov exponents. *Geophys. Res. Lett.* **31**, L17203 (2004).

17. Haller, G. & Yuan, G. Lagrangian coherent structures and mixing in two-dimensional turbulence. *Physica D* **147**, 352–370 (2000).
18. d’Ovidio, F., Isern, J., López, C., Hernández-García, E. & García-Ladona, E. Comparison between Eulerian diagnostics and Finite-Size Lyapunov Exponents computed from Altimetry in the Algerian basin. *Deep-Sea Res. I* **56**, 15–31 (2009).
19. Stramma, L., Johnson, G., Firing, E. & Schmidtko, S. Eastern Pacific oxygen minimum zones: Supply paths and multidecadal changes. *J. Geophys. Res.* **115**, C09011 (2010).
20. Czeschel, R., Stramma, L., Schwarzkopf, F., Giese, B., Funk, A. *et al.* Middepth circulation of the eastern tropical South Pacific and its link to the oxygen minimum zone. *J. Geophys. Res.* **116**, C01015 (2011).
21. Lehahn, Y., d’Ovidio, F., Lévy, M. & Heifetz, E. Stirring of the northeast Atlantic spring bloom: A Lagrangian analysis based on multisatellite data. *J. Geophys. Res.* **112**, C08005 (2007).
22. Sheskin, D. J. *Handbook of parametric and nonparametric statistical procedures*. (CRC Press, Boca Raton, 2003).
23. Shchepetkin, A. & McWilliams, J. The regional oceanic modeling system (ROMS): a split-explicit, free-surface, topography-following-coordinate oceanic model. *Ocean Model.* **9**, 347–404 (2005).

24. Gutknecht, E., Dadou, I., Marchesiello, P., Cambon, G., Vu, B. L. *et al.* Nitrogen transfers off Walvis Bay: a 3-D coupled physical/biogeochemical modeling approach in the Namibian upwelling system. *Biogeosciences* **10**, 4117–4135 (2013).
25. Montes, I., Schneider, W., Colas, F., Blanke, B. & Echevin, V. Subsurface connections in the eastern tropical Pacific during La Nina 1999-2001 and El Nino 2002-2003. *J. Geophys. Res.* **116**, C12022 (2011).
26. Liu, W. T., Tang, W. & Polito, P. S. NASA scatterometer provides global ocean-surface wind fields with more structures than numerical weather prediction. *Geophys. Res. Lett.* **25**, 761–764 (1998).
27. Da Silva, A., Young, C. & Levitus, S. *Atlas of Surface Marine Data 1994, vol. 1, Algorithms and Procedures, NOAA Atlas NESDIS 6*, (US Dep. of Commer., Washington DC, 1994).
28. Carton, J. A. & Giese, B. S. A reanalysis of ocean climate using Simple Ocean Data Assimilation (SODA). *Mon. Weather Rev.* **136**, 2999–3017 (2008).
29. Bettencourt, J. H., López, C. & Hernández-García, E. Oceanic three-dimensional Lagrangian coherent structures: A study of a mesoscale eddy in the Benguela upwelling region. *Ocean Modell.* **51**, 73–83 (2012).

Correspondence Correspondence and requests for materials should be addressed to JHB. (email:joao.bettencourt@ucd.ie).

Acknowledgements JHB, CL and EHG acknowledge support from FEDER and MINECO (Spain) through projects ESCOLA (CTM2012-39025-C02-01) and INTENSE@COSYP (FIS2012-30634). JHB acknowledges financial support of the Portuguese FCT (Foundation for Science and Technology) and Fundo Social Europeu (FSE/QREN/POPH) through the predoctoral grant SFRH/BD/63840/2009. IM would like to acknowledge the EUR-OCEANS Consortium for support through a Flagship post-doctoral fellowship to IM on deoxygenation in the oceans.

Competing Interests The authors declare that they have no competing financial interests.

Author Contributions JHB, CL, EHG, BD and VG directed the study; JHB, CL, EHG, BD, IM, JS, AP, VG analyzed data and performed numerical simulations; JHB, CL, EHG, VG, wrote the paper with significant contributions from BD.

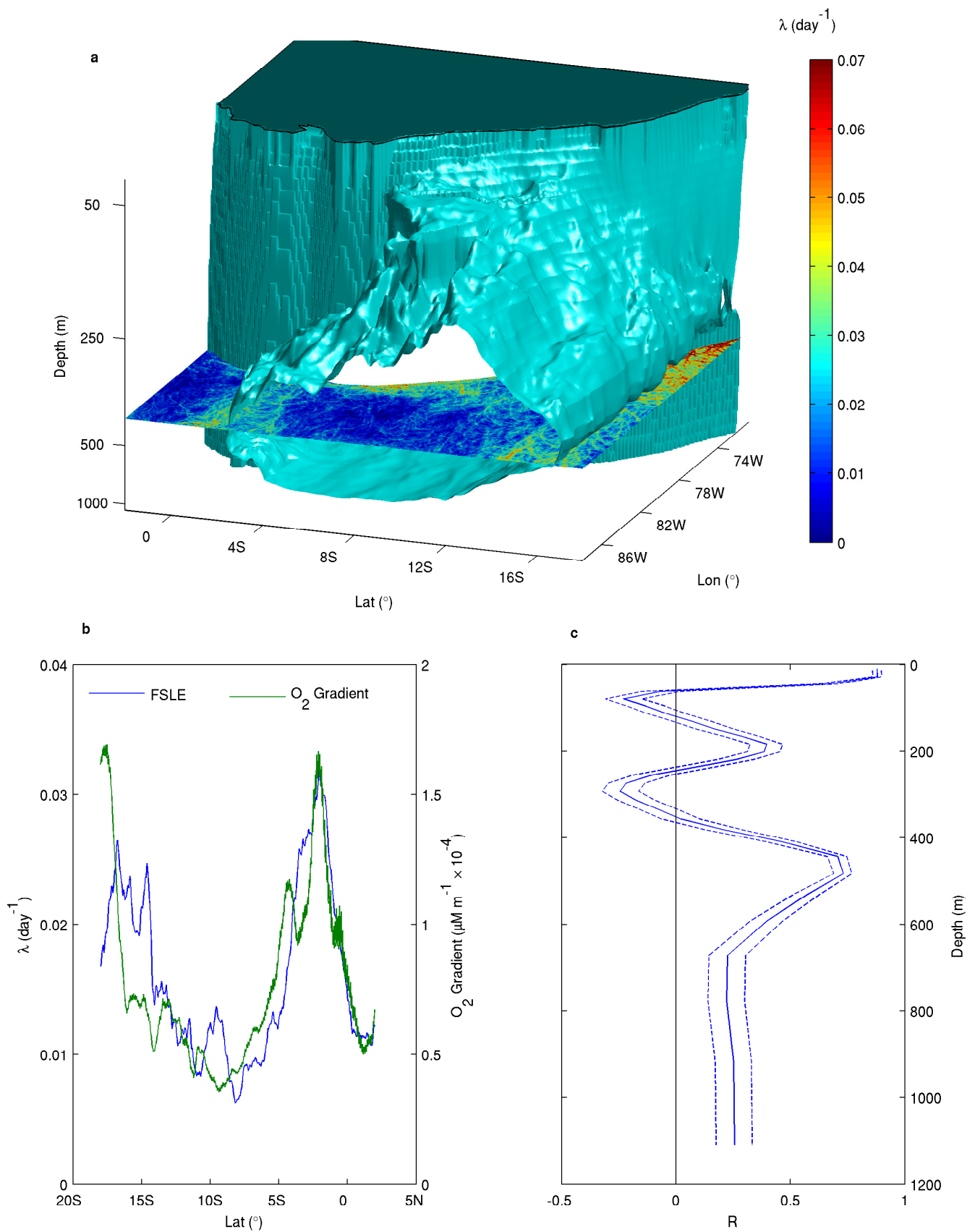


Figure 1: OMZ core, finite-size Lyapunov exponent (FSLE) and FSLE- O_2 gradient correlations for simulation year 21. a) $20 \mu M$ isosurface of mean O_2 concentration and the mean FSLE field at 410 meters depth. Note the stretched vertical scale. Flat top shows the Peruvian coast. b) Zonally averaged mean (z.a.m.) FSLE and O_2 gradient, averaged between 380 m and 600 m depth. c) Pearson correlation coefficient (R) between z.a.m. FSLE and O_2 gradient (solid line). Fisher 95% confidence interval on R (dashed line).

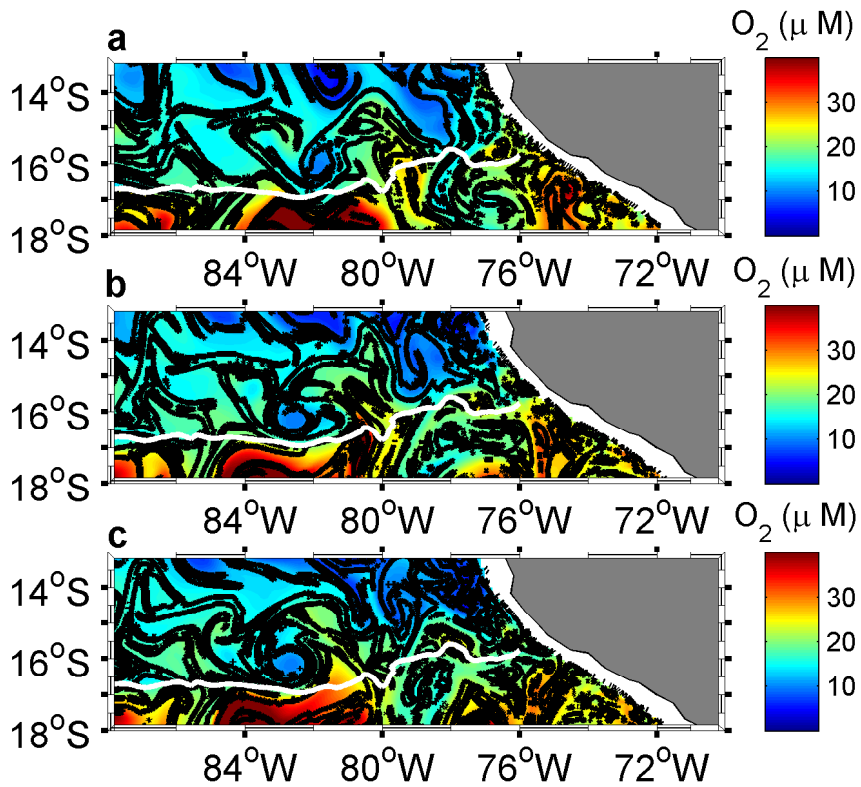


Figure 2: Entrainment of O_2 rich waters into the OMZ due to the motion of Lagrangian coherent structures. Color codifies O_2 at 410 m depth and the lines are the 0.075 day^{-1} FSLE isolines. a) 16 September; b) 7 October; c) 25 October; all of s.y. 21. Note the oxygen-rich tongue entering the OMZ at $80-82^\circ W$. White continuous line is the $20 \mu M$ mean isoline at 410 m depth (corresponding to the southern OMZ boundary).

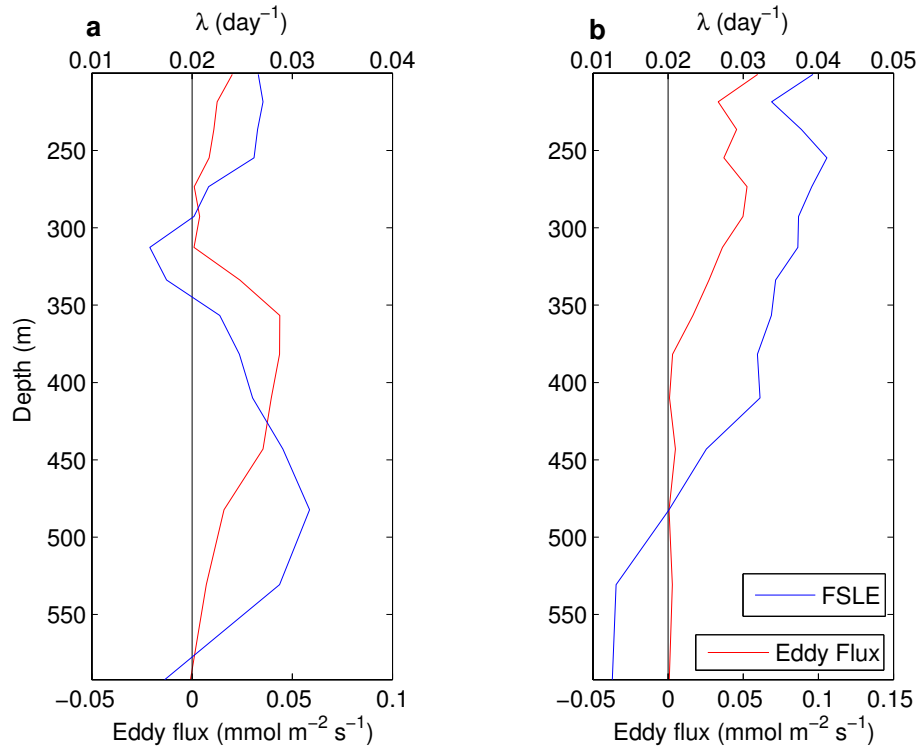


Figure 3: Vertical profiles of FSLE and O₂ eddy fluxes from 200 to 600m. Mean FSLE (blue lines) and normal O₂ eddy flux (red lines) averaged from the coast until 88° W for each depth and during simulation year 21 at (a) Northern 20 μM mean boundary and (b) Southern 20 μM mean boundary. Positive fluxes bring O₂ into the OMZ. The vertical line indicates the zero value for the fluxes.

Boundaries of the Peruvian Oxygen Minimum Zone shaped by coherent mesoscale dynamics.

Supplementary Information

by João H. Bettencourt^{*1,2}, Cristóbal López¹, Emilio Hernández-García¹, Ivonne Montes^{3,6}, Joël Sudre⁴, Boris Dewitte⁴, Aurélien Paulmier^{4,5}, and Véronique Garçon⁴

¹ IFISC, Instituto de Física Interdisciplinar y Sistemas Complejos (CSIC-UIB), Campus Universitat de les Illes Balears, E-07122 Palma de Mallorca, Spain.

² School of Mathematical Sciences, University College Dublin, Dublin 4, Ireland.

³ GEOMAR, Helmholtz-Zentrum für Ozeanforschung Kiel, Wischhofstr. 1-3, 24148 Kiel, Germany.

⁴ LEGOS, Laboratoire d'Etudes en Géophysique et Océanographie Spatiales, 18, av. Edouard Belin, 31401 Toulouse Cedex 9, France.

⁵ IMARPE, Instituto del Mar de Perú, Esquina Gamarra y General Valle S/N, Chucuito, Callao, Perú.

⁶ IGP, Instituto Geofísico del Perú, Lima, Perú.

Backward FSLE three-dimensional fields

Here we give additional details on the calculation of the finite-size Lyapunov exponent (FSLE) fields and further discuss their horizontal and vertical structure. Maximum values of FSLE computed backwards in time can be interpreted as fronts of advected tracers, since they delineate the lines along which the tracers are stretched and folded by the fluid flow. By the same reason, they provide barriers to transport with little or no flow across them [1, 2].

We computed daily three dimensional ($3d$) fields of backward FSLE for simulation year 21. This was done by setting up a regular $3d$ latitude-longitude-depth

grid of initial conditions with spacing in the two horizontal directions of $\delta_0 = 1/27^\circ$ (i.e. ≈ 4 km) and 30 vertical layers with variable vertical spacing. The grid covered the eastern tropical south Pacific (ETSP) from 88° W to 70° W and 18° S to 2° N. Vertically, the grid extended from 10 to 1100 m depth and was clustered in the upper 500 m of ocean. To obtain the FSLE field, $\lambda(\mathbf{x}, t)$, at location \mathbf{x} and time t , one particle is released at time t from grid node at location \mathbf{x} and the separation to the particles released from neighboring nodes is monitored. τ is the time needed for the first of these separations to reach the value δ_f (that in this study was set at 100 km). Trajectories were integrated backward in time for 6 months with a Runge-Kutta 4th order method. If at the end of this interval the separations are smaller than δ_f , or if the particles leave the domain or hit the shore, then the FSLE for the release location is set to zero. Otherwise, the FSLE is computed as

$$\lambda(\mathbf{x}, t) = \frac{1}{\tau} \log \frac{\delta_f}{\delta_0}.$$

A map of instantaneous backward FSLE is shown in Fig. S1 for different depths. In the upper layer (Fig. S1 a) we observe that south of 4° S the FSLE field is organized in thin filamental features with high FSLE values superimposed on a low FSLE background. North of 4° S, we see a larger density of small-scale features, that represent the change in dynamical regime [3] as we approach the equator. Time scales associated with the Lagrangian dynamics at this depth vary from 4 to 10 days (the FSLE is roughly an inverse time scale). At larger depths (Fig. S1 b, c and d) the features of the instantaneous FSLE field are maintained although the intensity is reduced from its values at the surface. The area near the equator with dense small-scale structure is reduced at 113 m depth and qualitatively different and shifted south at 410 and 592 m depth (Fig. S1 b, c and d, respectively). At all depths

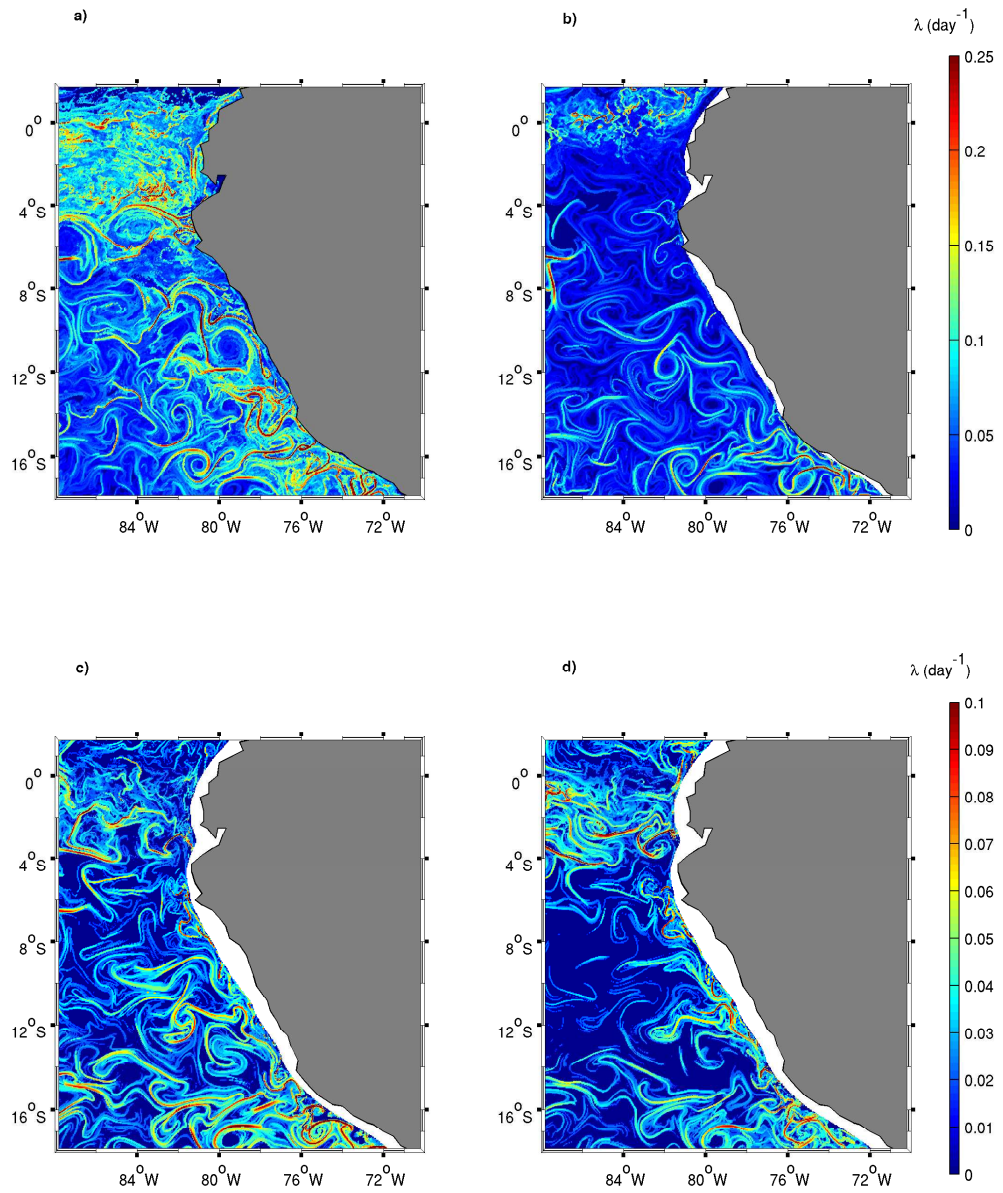


Figure S1: Map of backward FSLE for the 1st of January of simulation year 21. a) 10 m depth. b) 113 m depth. C) 410 m depth. D) 592 m depth. Note the different colorbar at different depths.

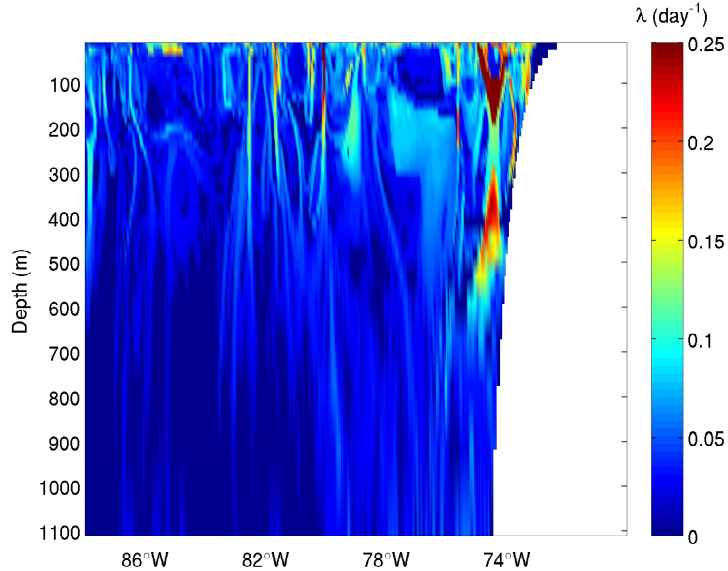


Figure S2: Vertical map of backward FSLE for the 1st of January of simulation year 21, at 16.45° S.

shown, the high FSLE lines are more common near the coast, which in this region is the main source of mesoscale variability due to instability of coastal currents and the associated upwelling regime [4, 5].

The vertical structure of the instantaneous FSLE field is shown in Fig. S2 for the same date on a vertical section at 16.45° S. The thin filamental structures appearing in the horizontal maps have a vertical extension of about 400 m from the surface down. The structures oriented parallel to the zonal axis reveal this *curtain-like* shape, as can be observed between 76° W and 78° W and 100 and 300 m depth. Such shape has already been observed (in 3d) in similar calculations for the Benguela upwelling zone [6] and can be understood theoretically [7]. Dynamical studies with particle trajectories showed that the most intense *curtains* can be related to Lagrangian eddy boundaries.

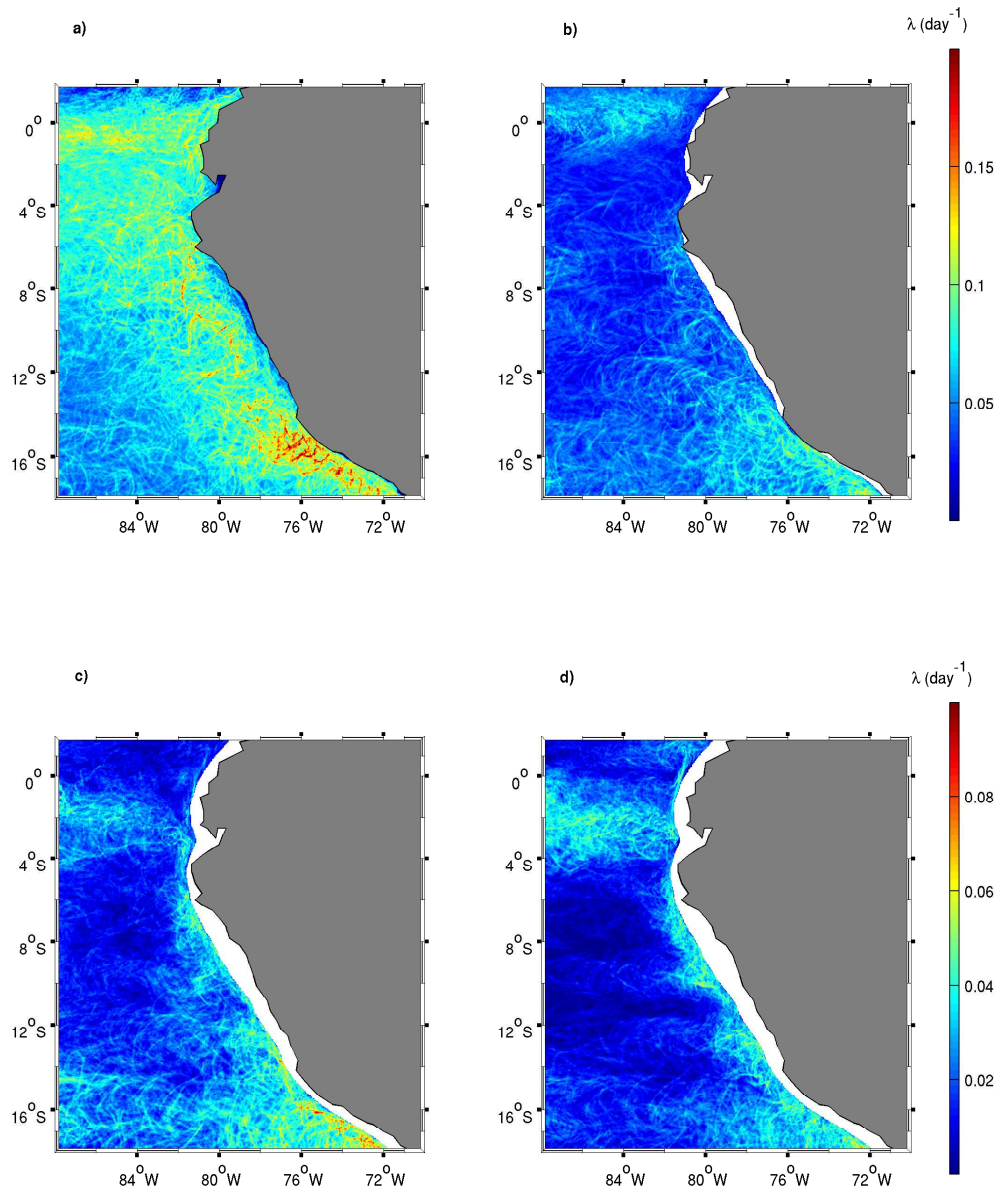


Figure S3: Horizontal maps of backward FSLE temporally averaged for simulation year 21. a) 10 m depth. b) 113 m depth. c) 410 m depth. d) 592 m depth. Note the different colorbar at different depths.

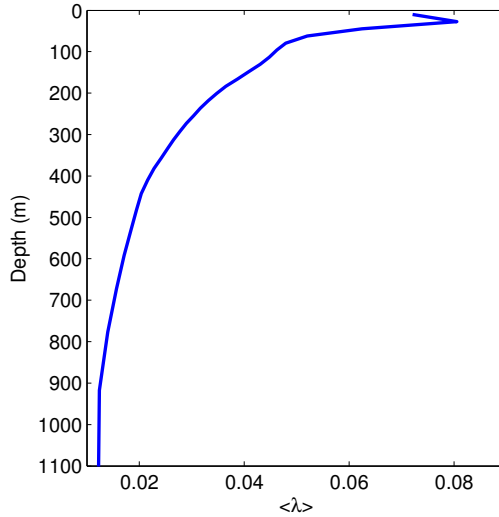


Figure S4: Time mean of the horizontally averaged depth profile of the backward FSLE field $\langle \lambda \rangle$ (in day^{-1}) for year 21.

The temporal-mean horizontal maps of the backward FSLE fields are shown in Fig. S3 for four depths: 10, 113 and 410 and 592 m. One can observe the most persistent patterns of mixing, in particular, the northern and southern strips delineating the boundaries of the oxygen minimum zone (OMZ). The depth profile of horizontally averaged mean FSLE field for simulation year 21 (Fig. S4) shows the decrease in stirring with depth, with a subsurface peak at ≈ 30 m depth. This decrease of stirring with depth, as measured by the FSLE, was also found in a study of the Benguela upwelling region [6]. Its origin could be simply the overall smaller velocities found at deeper layers, and also the decrease in the nonlinearity of the mesoscale eddies (as indicated for example by its ratio between rotation and propagation velocities) that occurs with depth [5].

Residence times

Residence times (RT) are a tool to study fluid exchange between two regions. Although the OMZ does not constitute a geographically determined region such as a basin or bay, it is still possible to define appropriate limits to the OMZ (as we have done all along this paper) so that fluid exchange between the OMZ and its exterior may be studied with RT distributions [8, 9]. They are a Lagrangian diagnosis complementary to the FSLE methods. The RT of a fluid particle is defined as the time it spends inside a certain region before crossing a particular boundary. Here we compute the RT in the OMZ as the time the particle remains with a O_2 content below $20 \mu M$. The results obtained are similar if instead we compute the exit time from the average OMZ core region, i.e. the volume in which the temporally averaged O_2 concentration is smaller than $20 \mu M$. Trajectories can be integrated forward in time (and then the computed time is properly an exit time) or backward in time (so that one is calculating then the time the particle has been in the region before the present moment).

We show in Fig. S5 the RT distribution at 410 meters depth for the 1st of July of simulation year 20. Similar results are observed at other depths. To obtain this distribution, particles were released from the same horizontal regular grid described in the previous section and the trajectories were integrated backward and forward for 2.5 years (the need to use such large integration times forced us to use as initial time the simulation year 20 instead of year 21 as in other calculations, since the simulation dataset contains only 22 years). Backward and forward FSLE fields were also computed for this date and location for comparison purposes.

The RT are larger than 2.5 years in most of the area identified as the OMZ core. In contrast with this rather homogeneous distribution in the centre, at the

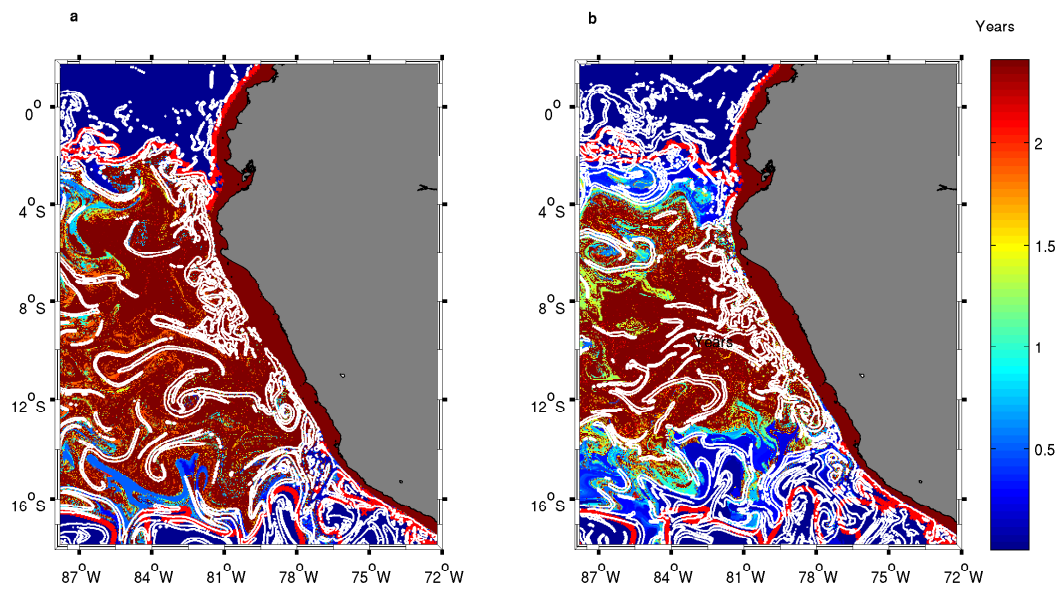


Figure S5: Residence times (RT) at 410 m depth for 1st July of simulation year 20. a) Backward RT. Superimposed white lines are $0.035\ day^{-1}$ backward FSLE isolines. b) Forward RT. Superimposed white lines are $0.038\ day^{-1}$ forward FSLE isolines. The magenta lines bound the region inside which the concentration of O_2 was smaller than $20\mu M$ already at the initial time, so that outside these lines the exit times are zero. The red color associated to a residence time of 2.5 years is in fact associated also to all residence times larger than this duration.

OMZ boundaries the RT distribution exhibits quite complex shapes, with several re-entrant zones of low RT and sharp transitions to low RT. Additionally, there are several cases of thin regions of low RT intruding in to the high RT central zone. These sharp boundaries between high and low RT coincide in some areas with high FSLE values. This coincidence is a feature observed with the RT distributions of passive particles in a given geographical region [9]. Since passive particles are Lagrangian tracers, we conclude that in the areas of matching RT changes and FSLE lines, the O_2 content is conserved along particle trajectories and local changes in O_2 occur mostly due to advection. The long residence times found are consistent with the low ventilation regime accompanied with biogeochemical processes which reduce oxygen concentrations to hypoxic levels.

Horizontal O_2 gradients

Here we enlarge our discussion on the relationship between FSLE and O_2 horizontal gradients. First we observe in Fig. S6 a) how the lines of high FSLE values determine instantaneous (at depth 410 m) fronts for the O_2 concentrations. These are located in the northern and southern boundaries of the OMZ as has been discussed all along the text. In Fig. S6 B) it is shown how the high-FSLE lines coincide with the largest horizontal gradients of O_2 .

In Fig. S7 a) and b) we show FSLE and O_2 gradient maps, respectively, averaged temporally (for simulation year 21) and vertically in the mid-depth range of the OMZ (between 350 and 600 m). We do not discuss the relationship between the high values of FSLE and of O_2 gradients found very close to the coast, since that region has very distinct dynamics and biogeochemistry, and it is influenced by the presence of

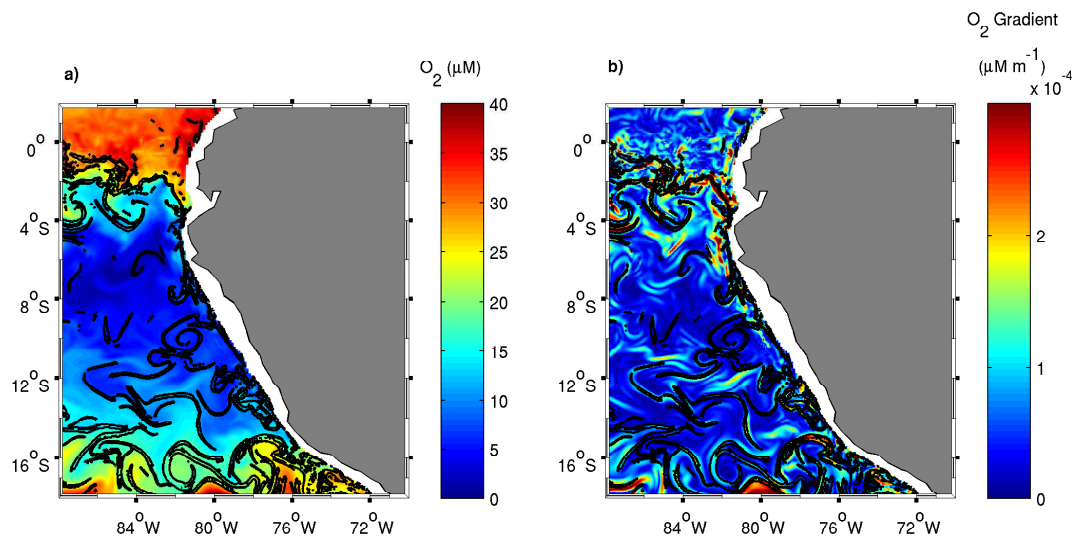


Figure S6: Lines of high FSLE values ($> 0.04 \text{ day}^{-1}$, black) superimposed on instantaneous O₂ and O₂ gradient fields on 1st of March of year 21 at 410 m depth. a) O₂ concentration. b) O₂ horizontal gradient.

coastal currents and water-column sediments interaction. The maps clearly show the high gradient zones north and south of a central basin with low average O_2 gradient that coincides with the OMZ. The northern band is located approximately at an interface between an eastward mean zonal flow relatively rich in O_2 [10, 11] and a southern adjacent westward mean flow. This flow configuration at middepth present in our simulation data shows similarities with ADCP data [12] taken in February 2009 that shows the SICC (South Intermediate Counter Current) eastward flow and the adjacent SEIC (South Equatorial Intermediate Current) westward flow with velocities about 2.5 cm/s . The mean FSLE field for the same depth range (Fig. S7 a) shows that the band between 0° and 4° S is a zone of high FSLE. On the southern boundary, high O_2 gradients are located close to the equatorward edge of the southern subtropical gyre, along a zonal band below 16° S. In this region, we also find high values of the mean FSLE but these are distributed along a wider zonal region, poleward from 14° S.

The center of the OMZ forms a basin of low O_2 gradients and also low FSLE. The low values of O_2 are due to low or inexistent ventilation (as quantified by large residence times) of this region coupled to the respiration of sinking organic matter. The low FSLE distribution is due to the absence of significant mesoscale activity at this depth. Although this region is located offshore of the Peru upwelling strip, and receives anticyclonic eddies formed by instability of the coastal currents [13], mesoscale activity as measured by eddy intensity decreases as we move offshore [5], and it is only intense in the two strips surrounding the OMZ.

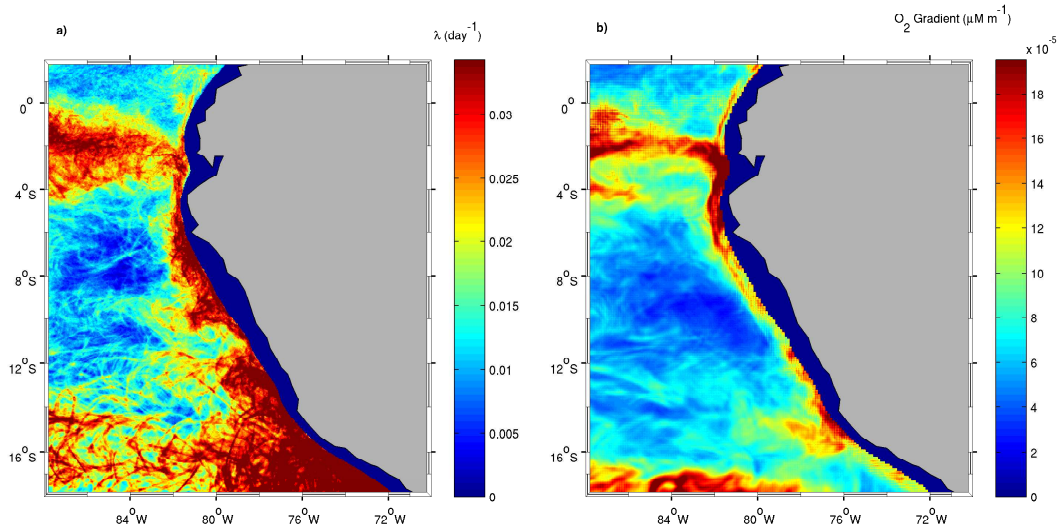


Figure S7: Mean fields averaged over 300 – 600 meters depth and during year 21. a) FSLE. b) O_2 horizontal gradient.

Physical and biogeochemical variability of O_2

Biogeochemical fluxes undergo a sharp decrease in variability around 300 m of depth, as evidenced from Figure 7 of [14]. That figure clearly indicates that the variability of physical fluxes becomes two orders of magnitude larger than that of biogeochemical fluxes below ~ 300 m, since the ratio is $\sim 1\%$ and lower. Therefore, O_2 can be considered as a passive tracer below 300 m. The ratio of variabilities (quantified as root mean square values) of physical and biogeochemical fluxes at 12°S is shown in Fig. S8. The dataset used is the same as that described in the Methods section of the main text, and physical and biological fluxes are identified from the terms of physical and biological origin in the balance equation for oxygen concentration.

Again, Fig. S8 highlights that below 300 m the variability in biogeochemical

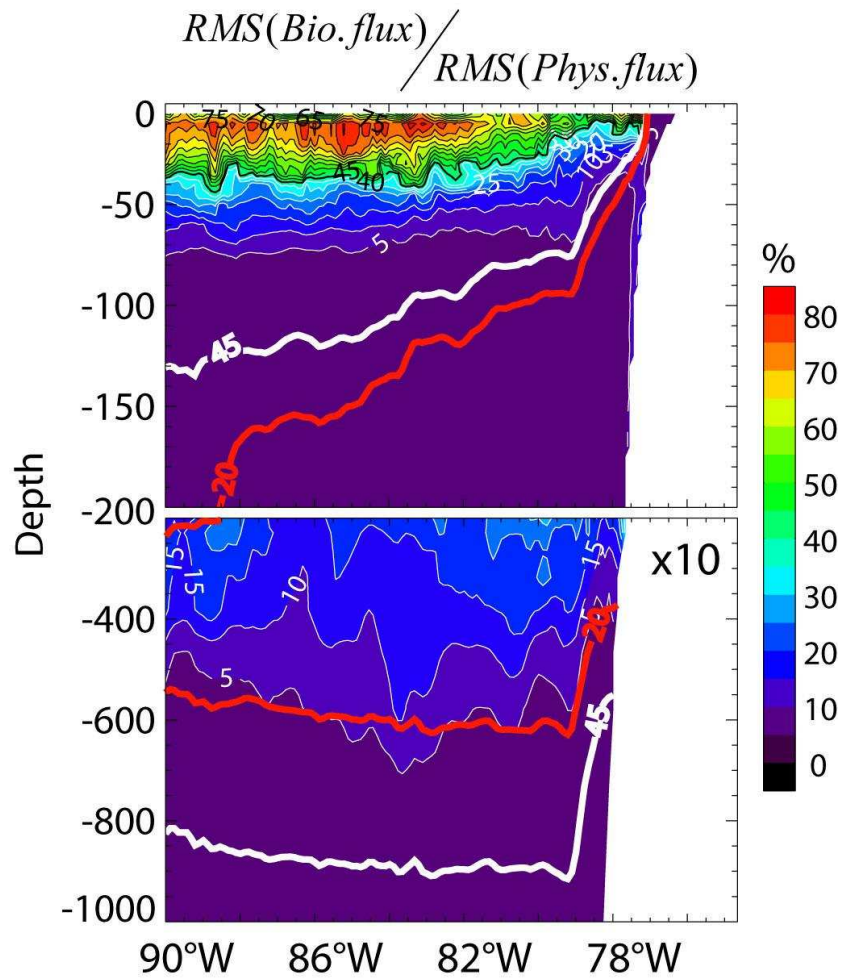


Figure S8: Ratio (in %) of the variability in the biogeochemical fluxes versus the variability of the physical flux along a vertical section at 12°S. The color bar applies to the upper panel, and the colors and values of the ratio in the lower panel correspond to values multiplied by 10 to highlight the vertical variability. The 45 μM (white line) and 20 μM (red line) O_2 isolines are also shown.

fluxes becomes two orders of magnitude smaller than the physical ones. We note that over the whole OMZ, variability in physical fluxes remains in general larger than the variability in biogeochemical fluxes, but small biological changes in O_2 can still diminish correlations between physical stirring and O_2 . Below 300 m the ratio between fluxes drops below 1% so that one can consider that below this depth the physical fluxes strongly dominate over biogeochemical processes. This is consistent with our observations, reported in the main text, of strong correlations between physical stirring and O_2 distributions in the range 380-600 m, whereas this correlation is not so strong at upper layers. To illustrate what is happening near the OMZ boundaries, we calculated the proportion of explained variance by the physical fluxes at different depths. The proportion of total variance (Var) in the O_2 change rate explained by the physical flux can be written (using that the total flux is the sum of the physical and the biogeochemical ones) as [15]:

$$R_{Phys}^2 = 1 - \frac{Var[\text{Biogeochemical flux}]}{Var[\text{Total flux}]}. \quad (1)$$

R_{Phys}^2 is shown in Fig. S8 at two depths (112m and 465m) corresponding to different zones of the OMZ. At 112 m, the biogeochemical fluxes, although having lower amplitude than the physical ones, can still contribute to generate local O_2 gradients which can influence advection terms. However at 465 m, the biogeochemical fluxes (within the OMZ) are almost two orders of magnitude lower than the physical flux (see Fig. S8 Fig. 7 of [14]). Fig. S9 shows that physical fluxes dominate over most of the study region, but they are more intense near the OMZ latitudinal boundaries. This is more remarkable at 465m than at 112m, which indicates that the lower correlation between the FSLE field and mean O_2 gradient at the surface may arise from the relative larger contribution of biogeochemical fluxes to the rate

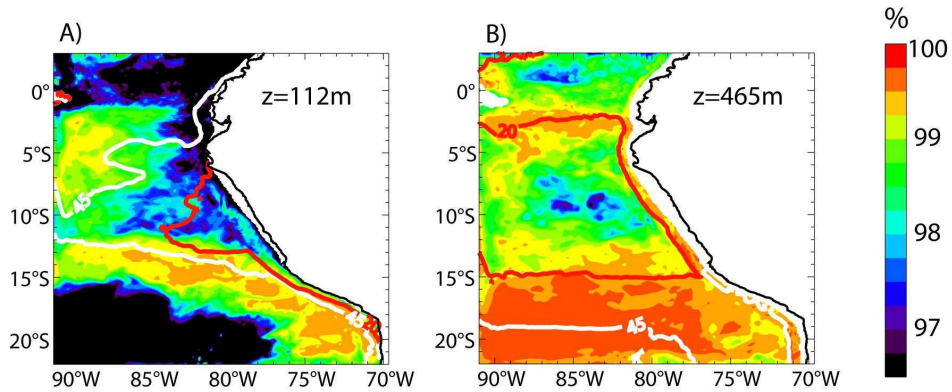


Figure S9: Explained variance of the physical flux with respect to the rate of O_2 change in % at A) 112m and B) 465m. The white (red) thick line indicates the iso-oxygene contour at $45 \mu M$ ($20 \mu M$)

of O_2 change there.

Eddy fluxes of O_2

We computed O_2 eddy fluxes by using the Reynolds transport theorem and the decomposition of the velocity and O_2 concentration fields in their mean and fluctuating components. Other physical fluxes such as small-scale turbulent diffusion turn out to be smaller. The eddy flux across each of the mean $20 \mu M$ north and south boundaries was computed by averaging the product of the fluctuating velocity component normal to the boundary in the horizontal and in the vertical directions and the fluctuating O_2 concentration component, thereby obtaining horizontal and vertical eddy fluxes. The sign of the normal was chosen so that a positive horizontal flux indicates transport towards the interior of the OMZ. For comparison purposes, mean horizontal and vertical fluxes were also computed from the mean velocity normal to the boundaries and the mean O_2 concentration. The integration

of the fluxes over the whole frontier gives the flow rate of O_2 into the OMZ through those boundaries.

The profiles of mean and eddy horizontal fluxes across the $20 \mu M$ OMZ boundaries for depths between 200 and 600 meters were computed for simulation year 21 and shown in Fig. S10. The fluxes are averaged also along the horizontal extension of the boundary at each depth. Blue lines are for the northern boundary and red for the southern one. Overall, the mean fluxes are much smaller than the eddy ones. In the northern boundary, eddy fluxes and mean fluxes are both positive up to about 250 m depth highlighting the oxygen supply role the Equatorial under-current and the primary southern subsurface counter-current play for the Peru-Chile under-current. At deeper locations the eddy flux is again positive, and the mean flow slightly negative (i.e. pointing outside the OMZ). At the southern border the eddy flux is positive above 380 m, becoming negligible further down. The mean flux is positive above about 230 m, being negative or negligible below. The total mean horizontal O_2 flow rates (Table S1) at the northern and southern boundaries are negative whereas the eddy flow rates are positive. At both OMZ boundaries, mesoscale turbulence tends to transport O_2 into the OMZ at a much higher rate than the mean flow removes O_2 from the OMZ. At the southern boundary computed flow rates are higher than at the northern boundary probably due to the longer horizontal extension of the southern boundary. The vertical eddy and mean O_2 flow rates (Table S2) turn out to be about one thousand times smaller than the horizontal ones, so that the discussion above for the horizontal fluxes applies indeed also to the total fluxes. Vertical fluxes show also magnitude differences between eddy and mean values.

To further investigate the correlation between FSLE and O_2 eddy flux, we singled

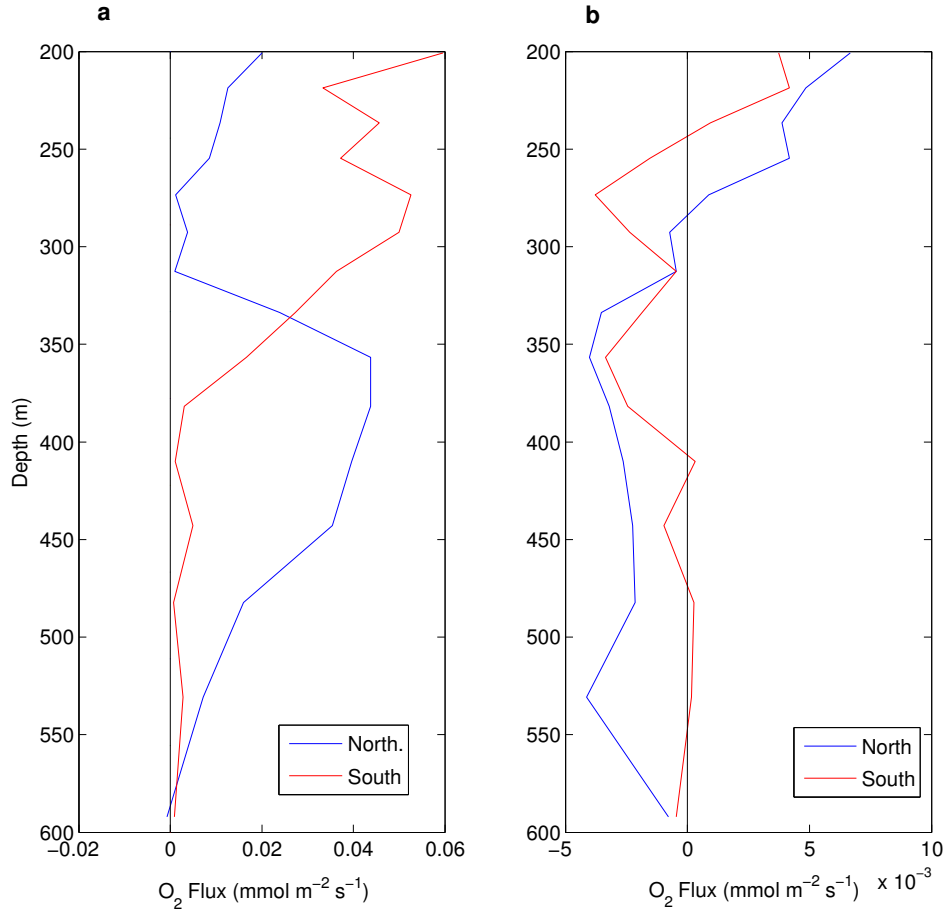


Figure S10: Vertical profiles of horizontal O₂ fluxes at the 20 μM OMZ mean boundaries between 200 and 600 m depth. The fluxes have been averaged along the horizontal extension of the boundary (from coast to 88°W) for each depth, and during simulation year 21. a) Eddy flux profile (these are the red curves in Fig. 3 of the main text). b) Mean flux profile (note the much smaller values as compared with the eddy fluxes.)

Boundary	Eddy ($\mu\text{mol s}^{-1}$)	Mean ($\mu\text{mol s}^{-1}$)
Northern	6.15×10^6	-2.01×10^5
Southern	1.00×10^7	-3.56×10^5

Table S1: Horizontal eddy and mean O₂ flow rates across the 20 μM mean boundaries from 200 to 600 m depth and from coast to 88°W, averaged over simulation year 21.

Boundary	Eddy ($\mu\text{mol s}^{-1}$)	Mean ($\mu\text{mol s}^{-1}$)
Northern	1197.0	16.5
Southern	-4226.4	-269.7

Table S2: Vertical eddy and mean O₂ flow rates across the 20 μM mean boundaries from 200 to 600 m depth and from coast to 88°W, averaged over simulation year 21.

out the contributions due to intraseasonal variability (timescales between 2-100 days, computed from the departure from monthly mean in the considered year 21) as opposed to the departures from the total annual mean used before. Indeed isolating the sole contribution of the O₂ eddy flux due to intraseasonal variability appeared interesting since FSLE might not capture stirring at the long seasonal timescales. In doing so, one finds an improved correlation between FSLE and O₂ horizontal eddy flux both at the northern and southern OMZ boundaries (linear correlation coefficient 0.47 versus 0.27 (north) and 0.79 versus 0.77 (south)).

Episodic ventilation events

We characterize the eventual entrainment of water across the OMZ boundaries by displaying in Fig. 11 Hovmöller plots of the time evolution of the O₂ anomaly at the North (panel a) and South (panel b) OMZ 20 μM boundaries at 410 m depth. The anomaly is the actual O₂ concentration minus the mean at that location (20 μM). Since the overall eddy fluxes point towards the OMZ interior, positive anomalies

indicate oxygenated water entering into the OMZ. The slopes in the Hovmöller plots indicate overall westward propagation.

O₂ anomalies are more variable for the northern (standard deviation of 4.8 μM) than for the southern boundary (standard deviation of 3.1 μM). At the Northern limit the O₂ front is more stable meaning that there is an available pool of O₂ rich waters readily available to be entrained into the OMZ core by propagating mesoscale structures. At the southern limit the O₂ anomaly seems to be dependent on the actual O₂ content of travelling eddies that occasionally approach the boundary.

At the northern border the anomalies last longer than at the southern one and remain more coherent during their propagation offshore. In the South, ventilation events are more intermittent. However, during the year under analysis, the greatest episode of O₂ anomaly crossing the OMZ at this depth occurred in the southern boundary with peak O₂ anomaly of $\sim 17 \mu M$ around day 300 and between 600 and 800 km from the coast (this is the episode depicted in Figure 2 of the main text).

Cross-wavelet spectra

As an alternative methodology to quantify correlations between O₂ concentrations and the stirring measure provided by FSLE we conducted a cross-wavelet analysis between the O₂ concentration and backward FSLE times series from our simulation dataset at three particular locations in order to identify the dominant time scales of co-variability. The locations were: BNDNORTH.OXYCLINE, located on the northern OMZ boundary (84°W,3°S) and 75 m depth; BNDNORTH.CORE, located in the OMZ core (84°W,3°S) at 410 m depth; and BNDSOUTH.CORE, in the southern boundary (84°W,16°S) at 410 m depth.

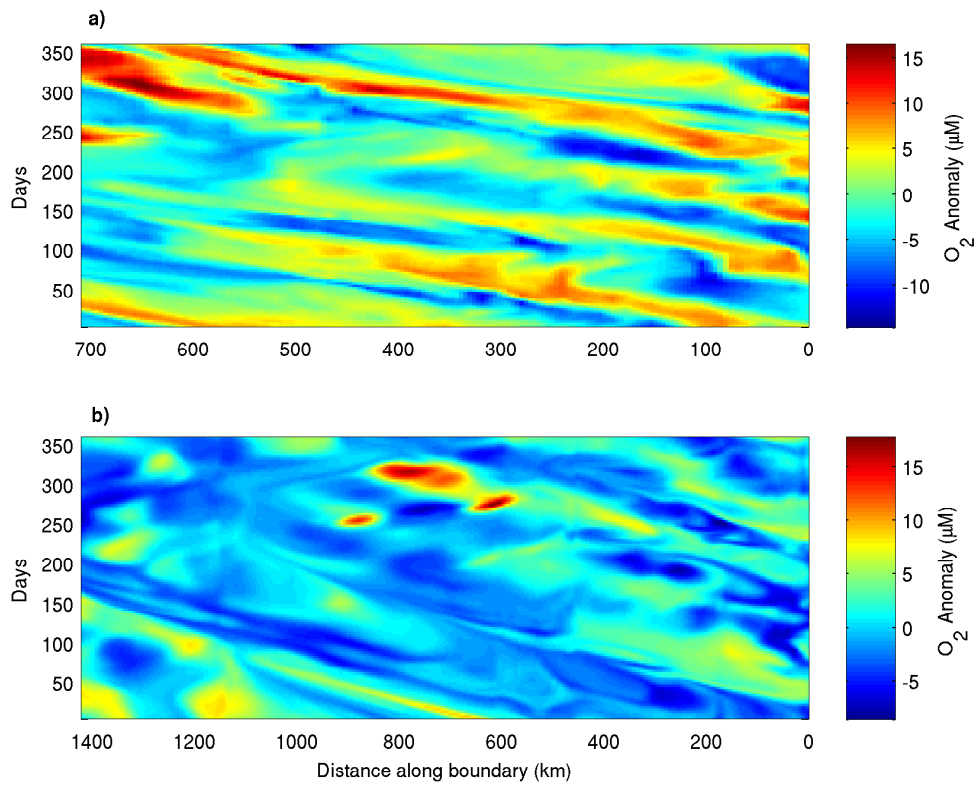


Figure S11: Hovmöller plots of O_2 concentration anomalies at OMZ boundaries at 410 m depth during simulation year 21. a) Northern boundary. b) Southern boundary. Anomaly measured relative to $20 \mu M$ level. Distance along boundary increases towards offshore, coast is at the right and the anomalies propagate offshore.

The climatological wavelet spectra consist in a wavelet decomposition of the intraseasonal anomaly time series followed by a calculation of the climatology of the wavelet power coefficient at each frequency. Wavelet spectra of O_2 and backward FSLE signals were computed following [16] at the three geographical locations. The time span of the signal is 4 years, from 1st July of simulation year 18 to 30 June of simulation year 22. Intraseasonal anomalies were estimated as the departures from the monthly mean. Wavelet power was normalized following Eq. 14 of [16] in order to compare the magnitude of the wavelet power at different frequencies. The mother wavelet used was the Morlet wavelet [16].

The climatology of the resulting cross-wavelet power is shown in Fig. S12. The plots indicate where the energy is dominant, i.e. where a significant covariance between O_2 and FSLE is present, as a function of calendar month. Large energy is found in the intraseasonal frequency band with significant peak energy around 45 days. The marked seasonality of the intraseasonal activity indicates a link with the seasonal modulation of the baroclinic instability of the coastal currents (i.e. the Peru undercurrent) during Austral summer and in the South during Austral winter[17].

Analyzing the dependence of the O_2 signal variability with stirring variability, i.e. FSLE levels, is out of the scope of this study. This could in principle be achieved as in [18], namely by artificially decreasing the strength of the non-linear terms in the momentum equation and measuring the resulting change in the variability in O_2 .

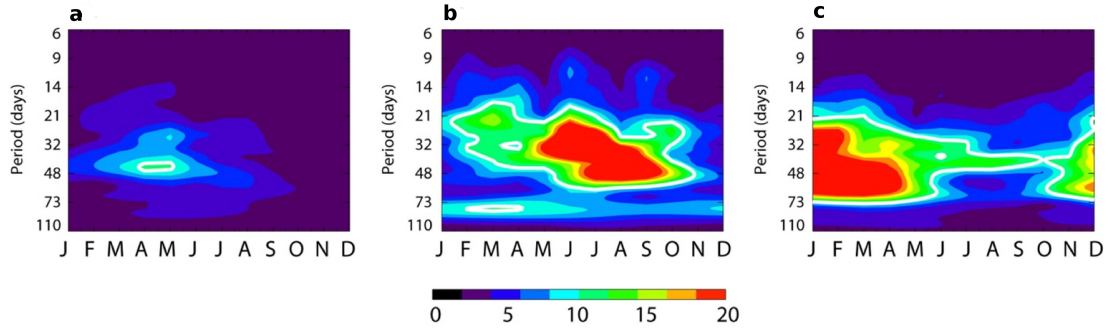


Figure S12: Climatological normalized cross-wavelet spectrum of O_2 concentration and FSLE time series at (a) BNDNORTH_CORE, (b) BNDSOUTH_CORE and (c) BNDNORTH_OXYCLINE. The horizontal axis indicates the calendar month. Units of the colorbar are $0.8 \times 10^{-4} M \text{ day}^{-1}$. The white thick contour in all panels indicates the 95% confidence level.

References

- [1] d’Ovidio, F., Fernández, V., Hernández-García, E. & López, C. Mixing structures in the Mediterranean Sea from finite-size Lyapunov exponents. *Geophysical Research Letters* **31**, L17203 (2004).
- [2] d’Ovidio, F., Isern, J., López, C., Hernández-García, E. & García-Ladona, E. Comparison between Eulerian diagnostics and Finite-Size Lyapunov Exponents computed from Altimetry in the Algerian basin. *Deep-Sea Res. I* **56**, 15–31 (2009).
- [3] Theiss, Jürgen. Equatorward Energy Cascade, Critical Latitude, and the Pre-eminence of Cyclonic Vortices in Geostrophic Turbulence. *Journal of Physical Oceanography* **34**, 1663–1678 (2004).
- [4] Penven, P., Echevin, V., Pasapera, J., Colas, F. & Tam, J. Average circulation, seasonal cycle, and mesoscale dynamics of the Peru Current System: A

- modeling approach. *Journal of Geophysical Research* **110**, C10021 (2005).
- [5] Chaigneau, A., Gizolme, A. & Grados, C. Mesoscale eddies off Peru in altimeter records: Identification algorithms and eddy spatio-temporal patterns. *Progress in Oceanography* **79**, 106–119 (2008).
- [6] Bettencourt, J. H., López, C. & Hernández-García, E. Oceanic three-dimensional Lagrangian coherent structures: A study of a mesoscale eddy in the Benguela upwelling region. *Ocean Modell.* **51**, 73–83 (2012).
- [7] Branicki, M., Mancho, A. M. & Wiggins, S. A Lagrangian description of transport associated with a front-eddy interaction: Application to data from the North-Western Mediterranean Sea. *Physica D* **240**, 282–304 (2011).
- [8] Buffoni, G., Falco, P., Griffa, A. & Zambianchi, E. Dispersion processes and residence times in a semi-enclosed basin with recirculating gyres: An application to the Tyrrhenian Sea. *Journal of Geophysical Research: Oceans* **102**, 18699–18713 (1997).
- [9] Hernández-Carrasco, I., López, C., Orfila, A. & Hernández-García, E. Lagrangian transport in a microtidal coastal area: the Bay of Palma, island of Mallorca, Spain. *Nonlinear Processes in Geophysics* **20**, 921–933 (2013).
- [10] Stramma, L., Johnson, G., Firing, E. & Schmidtko, S. Eastern Pacific oxygen minimum zones: Supply paths and multidecadal changes. *Journal of Geophysical Research* **115**, C09011 (2010).
- [11] Montes, I., Colas, F., Capet, X. & Schneider, W. On the pathways of the equatorial subsurface currents in the eastern equatorial Pacific and their con-

- tributions to the Peru-Chile Undercurrent. *Journal of Geophysical Research* **115**, C09003 (2010).
- [12] Czeschel, R., Stramma, L., Schwarzkopf, F., Giese, B., Funk, A. *et al.* Middepth circulation of the eastern tropical South Pacific and its link to the oxygen minimum zone. *Journal of Geophysical Research* **116**, C01015 (2011).
- [13] Chaigneau, A., Le Texier, M., Eldin, G., Grados, C. & Pizarro, O. Vertical structure of mesoscale eddies in the eastern South Pacific Ocean: A composite analysis from altimetry and Argo profiling floats. *J. Geophys. Res.* **116**, C11025 (2011).
- [14] Montes, I., Dewitte, B., Gutknecht, E., Paulmier, A., Dadou, I. *et al.* High-resolution modeling of the Eastern Tropical Pacific Oxygen Minimum Zone: Sensitivity to the tropical oceanic circulation. *Journal of Geophysical Research Oceans* **119**, 5515–5532 (2014).
- [15] Von Storch, H. & Zwiers, F. W. *Statistical analysis in climate research*. (Cambridge University Press, Cambridge, 2001).
- [16] Torrence, C. & Compo, G. P. A practical guide to wavelet analysis. *Bulletin of the American Meteorological Society* **79**, 61–78 (1998).
- [17] Echevin, V., Colas, F., Chaigneau, A. & Penven, P. Sensitivity of the Northern Humboldt Current System nearshore modeled circulation to initial and boundary conditions. *Journal of Geophysical Research: Oceans* **116**, C07002 (2011).
- [18] Gruber, N., Lachkar, Z., Frenzel, H., Marchesiello, P., Munnich, M. *et al.* Eddy-induced reduction of biological production in eastern boundary upwelling systems. *Nature Geoscience* **4**, 787–792 (2011).